

Estimating ocean tide loading displacements with GPS and GLONASS

Bogdan Matviichuk¹, Matt King¹, and Christopher Watson¹

¹School of Technology, Environments and Design, University of Tasmania, Hobart, 7001, Australia

Correspondence: Bogdan Matviichuk (bogdan.matviichuk@utas.edu.au)

Abstract. Ground displacements due to ocean tide loading have previously been successfully observed using GPS data, and such estimates for the principal lunar M_2 constituent have been used to infer the rheology and structure of the asthenosphere. The GPS orbital repeat period is close to that of several other major tidal constituents (K_1 , K_2 , S_2) thus GPS-estimates of ground displacement at these frequencies are subject to GPS systematic errors. We assess the addition of GLONASS to increase the accuracy and reliability of eight major ocean tide loading constituents: four semi-diurnal (M_2 , S_2 , N_2 , K_2) and four diurnal constituents (K_1 , O_1 , P_1 , Q_1). We revisit a previous GPS study, focusing on 21 sites in the UK and western Europe, expanding it with an assessment of GLONASS and GPS+GLONASS estimates. In the region, both GPS and GLONASS data are abundant since 2010.0. We therefore focus on the period 2010.0-2014.0, a span considered long enough to reliably estimate the major constituents. Data were processed with a kinematic PPP strategy to produce site coordinate time series for each of 3 different modes: GPS, GLONASS and GPS+GLONASS. The GPS solution with ambiguities resolved was used as a baseline for performance assessment of the additional modes. GPS+GLONASS shows very close agreement with ambiguity resolved GPS for lunar constituents (M_2 , N_2 , O_1 , Q_1) but with substantial differences for solar-related constituents (S_2 , K_2 , K_1 , P_1), with solutions including GLONASS being generally closer to model estimates. While no single constellation mode performs best for all constituents and components, we propose to use a combination of constellation modes to recover tidal parameters: GPS+GLONASS for most constituents except for K_2 and K_1 where GLONASS (north and up) and GPS with ambiguities resolved (east), perform best.

1 Introduction

Earth's gravitational interactions with the Sun and the Moon generate solid Earth and ocean tides. These tides produce periodic variations in both the gravity field and Earth's surface displacement. Additionally, the ocean tides produce a secondary deformational effect due to associated periodic water mass redistribution, known as Ocean Tide Loading (OTL) (e.g., Agnew, 2015; Jentzsch, 1997; Baker, 1984). OTL is observable in surface displacements (and their spatial gradients, i.e. tilt and strain) and gravity. Displacement and gravity attenuate approximately as the inverse of the distance from the point load while gradients have this relation but with distance squared (Baker, 1984). Thus, OTL displacement and gravity changes show greater sensitivity to regional solid Earth structure in comparison to tilt or strain observations (Martens et al., 2016), making this an observation of interest for studying solid Earth rheology.

Global Navigation Satellite Systems (GNSS) are particularly convenient for measuring OTL displacements due to the widescale deployment of dense instrument arrays. Data from continuous GNSS stations have been shown to provide estimates of OTL with sub-millimetre precision using two main approaches as described by Penna et al. (2015): the harmonic parameter estimation approach – OTL displacement parameters are solved for within a static GNSS solution (e.g., Schenewerk et al., 2001; Allinson, 2004; King et al., 2005; Thomas et al., 2006; Yuan and Chao, 2012; Yuan et al., 2013); and the kinematic approach – OTL constituents are predominantly estimated from high-rate kinematic GNSS-derived time series (e.g., Khan and Tscherning, 2001; King, 2006; Penna et al., 2015; Martens et al., 2016; Wang et al., 2020). In this paper, we follow the kinematic approach.

To date, GNSS-derived OTL displacements have been estimated using predominantly the US Global Positioning System (GPS). GPS-derived measurements of Earth-surface displacement at tidal periods have been successfully used to observe OTL displacement and validate ocean tide models (Urschl et al., 2005; King et al., 2005). The residual displacement between observed and predicted OTL has been related to deficiencies in ocean tide models, reference-frame inconsistencies, Earth model inaccuracies, the unmodelled constituents’ dissipation effect and systematic errors in GPS (e.g., Thomas et al., 2006; Ito and Simons, 2011; Yuan et al., 2013; Bos et al., 2015).

Recent studies have made use of GPS-derived OTL to study dissipation or anelastic dispersion effects in the shallow asthenosphere at the M_2 frequency (e.g. Bos et al., 2015). This type of investigation has not been easily done previously due to various limiting factors such as the accuracy of ocean tide models and the quality and availability of GPS observations. Recently, however, models have improved dramatically with the use of satellite altimetry (Stammer et al., 2014), and GNSS networks have both expanded and have improved data quality. Together, this has enabled the exploration of limitations in the global seismic Preliminary Reference Earth Model (PREM) (Dziewonski and Anderson, 1981) with GPS observations in the western United States (Ito and Simons, 2011; Yuan and Chao, 2012), western Europe (Bos et al., 2015), South America (Martens et al., 2016), Eastern China Sea region (Wang et al., 2020) and globally (Yuan et al., 2013). These limitations are associated partially with the incompatibility of the elastic parameters within the seismic (1 s period) and the tidal frequency bands and the anelasticity of the upper layers of the Earth, particularly the asthenosphere. The latter was studied through modelling the GPS-observed residuals of the major lunar tidal constituent, M_2 , by Bos et al. (2015) and, later, Wang et al. (2020), while Lau et al. (2017) used M_2 residual from the global study of Yuan et al. (2013) to constrain Earth’s deep-mantle buoyancy.

Previous studies have highlighted an apparently large error in solar-related constituents estimated from GPS, in particular K_2 and K_1 . This is in part due to their closeness to the GPS orbital (K_2) and constellation (K_1) repeat periods, which strongly aliases with orbital errors. The closeness to the GPS constellation repeat period may induce interference from other signals such as site multipath which will repeat with this same characteristic period (Schenewerk et al., 2001; Urschl et al., 2005; Thomas et al., 2006). Additionally, the P_1 constituent has a period close to that of 24 hours which is the timespan used for the IGS-standard orbit and clock products (Griffiths and Ray, 2009), and hence may be contaminated by day-to-day discontinuities present in the products (Ito and Simons, 2011).

Urschl et al. (2005) proposed that the addition of GLONASS (GLObal NAVigation Satellite System), a GNSS developed and maintained by Russia (USSR before 1991), could improve the extraction of K_2 and K_1 constituents as the orbit period of

the GLONASS satellites (~ 11 h 15 min 44 sec) and constellation repeat period (~ 8 days) are well separated from major tidal frequencies. However, for many years GLONASS suffered from an unstable satellite constellation and very sparse network of continuous observing stations. This has been progressively addressed over the last decade to the point where many national networks now include a high density of GLONASS (and other GNSS) receivers.

65 We seek to improve estimates of OTL displacement from continuous GNSS data, especially for constituents that are subject to systematic error in GPS-only solutions (e.g. S_2 , K_2 , K_1 , P_1) as found in previous studies (Allinson, 2004; King, 2006; Yuan and Chao, 2012). We do this by using both GLONASS and GPS data to estimate amplitudes and phases for the eight major OTL constituents (M_2 , S_2 , N_2 , K_2 , K_1 , O_1 , P_1 , Q_1). As in the very recent study of Abbaszadeh et al. (2020), our work focuses particularly on understanding the sensitivity of estimates to different processing choices, although our work focuses on quite
70 dense network in western Europe while their work focused on a globally-distributed set of stations.

2 Dataset

The sites used in our study are shown in Figure 1, with a focus on south-west England where a large M_2 OTL signal is present. Of the 21 stations, 14 stations are in south-west England: covering both sides of Bristol channel (ANLX, SWAS, CARI, CAMO, PADT, APPL, TAUT) and northern coast of English Channel up to Herstmonceux (PMTH, PRAE, EXMO,
75 PBIL, POOL, CHIO, SANO, HERT) with one site (BRST) in the south. Two sites are in northern England (WEAR, LOFT), two in Scotland (LERI, BRAE) with one site in central Europe (ZIM2). All sites are equipped with GPS+GLONASS receivers. Note that sites CAMO, LERI and ZIM2 sites replace CAMB, LERW and ZIMM respectively, which were used by Penna et al. (2015), to allow for use of GLONASS data recorded at the former set of sites.

Aside from the addition of GLONASS data, an important difference to the study of Penna et al. (2015) is the shift in time
80 period from 2007.0–2013.0 to 2010.0–2014.0. This shift provides sufficient GLONASS data following the upgrade of many receivers to track GLONASS from 2009 that followed the restoration of the GLONASS constellation finished in March 2010 (24 SVs). Despite this covering a shorter time span, the length of continuous observations at each site (minimum availability of 95% through the dataset) exceeds the recommended ~ 1000 days of continuous observations (4 years with 70% availability) (Penna et al., 2015). The selected time period is fully covered by a complete and homogeneous set of reprocessed orbit and
85 clock products.

The chosen sites experience a range of M_2 up OTL amplitudes, from > 30 mm (ANLX, APPL, BRST, CAMO, PADT, PRAE), 15–30 mm (CARI, EXMO, LOFT, PBIL, SWAS, TAUT) and < 15 mm (BRAE, CHIO, LERI, POOL, SANO, WEAR, ZIM2).

3 GNSS data processing strategy

90 The processing strategy was largely based on the GPS-only kinematic Precise Point Positioning (PPP) approach (Zumberge et al., 1997) as per Penna et al. (2015), but with important modifications in terms of the software and to permit the inclu-

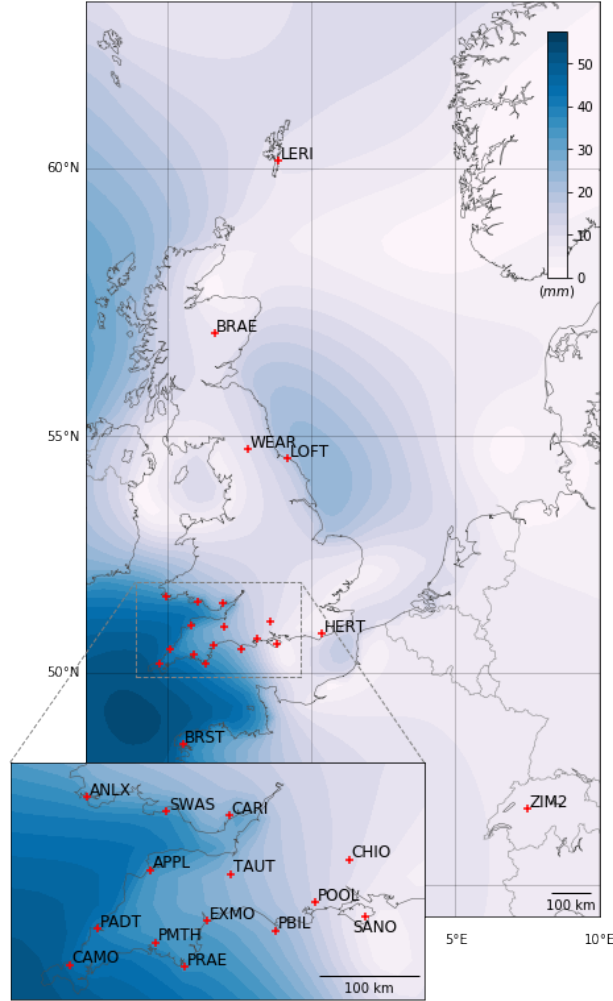


Figure 1. Map of the study area with GNSS site codes and M_2 up displacement amplitude in the background (TPXO7.2 ocean tide model and spherically symmetric earth with PREM structure).

sion of GLONASS data. We address PPP in three different modes here: GPS, GLONASS and combined GPS+GLONASS. In particular, we use NASA JPL's GipsyX (v1.3), which is a substantial rewrite of the now legacy GIPSY-OASIS code to allow for, amongst other things, multi-GNSS analysis. Penna et al. (2015) used GIPSY-OASIS v6.1.2. We adopted a PPP solution approach and estimated station positions every 5 minutes with a random walk model introducing estimated optimum between-epoch constraints on coordinate evolution. We used the VMF1 gridded troposphere mapping function, based on the European Centre for Medium-Range Weather Forecasts (ECMWF) numerical weather model (Boehm et al., 2006). Additionally, ECMWF values for the hydrostatic zenith delay and wet zenith delay were used as a priori values for stochastic estimation of the wet zenith delay as a random walk process with optimum process noise values (Sect. 4) and tropospheric gradients were

100 estimated as a random walk process (Bar-Sever et al., 1998), with process noise at 0.005 mm/sqrt(s). An elevation cut-off angle of seven degrees was applied, sufficient to maximize the number of GLONASS observations at the respective site latitude as noted by Abbaszadeh et al. (2020), together with observation weights that were a function of the square-root of the sine of the satellite elevation angle.

Earth body-tide (EBT) and pole tides were modelled according to IERS 2010 Conventions (Petit and Luzum, 2010). The
105 OTL displacement within each processing run was modelled with the FES2004 tidal atlas (Lyard et al., 2006) and elastic Green's functions based on the Gutenberg-Bullen Earth model (Farrell, 1972) (referred to as FES2004_GBe), with centre-of-mass correction applied depending on the adopted orbit products. The FES2004-based OTL values were computed using the free ocean tide loading provider that uses OLFG/OLMP software (<http://holt.oso.chalmers.se/loading>) while the rest of OTL values used in this publication were computed with CARGA software (Bos and Baker, 2005). We did not model atmospheric
110 S_2 tidal displacements.

PPP requires pre-computed precise satellite orbit and clock products for each constellation processed which should be solved for simultaneously within a single product's solution. Unfortunately, JPL's native clock and orbit products are not yet available for non-GPS constellations hence we adopted products from two International GNSS Service (IGS) (Johnston et al., 2017) Analysis Centres (ACs): the European Space Agency (ESA) and Centre for Orbit Determination in Europe (CODE). The ESA
115 combined GPS+GLONASS products from the IGS second reprocessing campaign (repro2) were used (Griffiths, 2019) while CODE's more recent REPRO_2015 campaign (Susnik et al., 2016) had to be used as CODE's repro2 are lacking separate 5 min GLONASS clocks.

All three products consist of satellite orbits and clocks, sampled at 15 and 5 minutes respectively, that were held fixed during our processing. The benefit of using JPL's native products, even though solely GPS, is the ability to perform PPP processing
120 with integer ambiguity resolution (AR). PPP AR in GIPSY-OASIS/GipsyX software packages can be performed by using wide lane and phase bias tables which are part of JPL's native products (Bertiger et al., 2010). To provide comparison with previous studies, GPS was processed with JPL's native orbit and clock products from the repro2 campaign (JPL's internal name is repro2.1) with AR.

The CODE and ESA clock and orbit products were generated in different ways. CODE's REPRO_2015 orbit positions were
125 computed using a 3-day data arc, while ESA used a 24-h data arc (Griffiths, 2019). Both ACs provided orbits in a terrestrial reference frame, namely IGS08 and IGB08, respectively, that are corrected for the centre of mass (geocentre) motion associated with OTL (FES2004 centre of mass correction) and are in the CE frame, following Fu et al. (2012). Alternatively, JPL products were generated from a 30-h data arc, and were computed with stations in a near-instantaneous frame realisation hence the orbits are in the CM frame (we note that the JPL products distributed by the IGS are, by contrast, in CE). Considering the above, the
130 modelled OTL values for JPL's native products solutions were corrected for the effect of geocentre motion while ESA/CODE products do not require this correction (Kouba, 2009).

It has been suggested that orbit arc length for a given product could potentially impact the estimated OTL displacements. In particular, Ito and Simons (2011) suggest that a 24-h data arc length (as per ESA products) may affect the P_1 constituent due to similarity of the periods. This is in addition to day-boundary edge effects given analysis of data in 24-h batches. We mitigate

135 these effects to some extent by processing the ground stations in 30-h batches (allowing 3-h either side of the nominal 24-h day boundary).

We post-processed the estimated coordinate time series as per Penna et al. (2015): the resulting 5-min sampled solutions were clipped to the respective 24-h window and merged together. Outliers were filtered from the raw 4-yr timeseries using two consecutive outlier-detection strategies: rejecting epochs with extreme receiver clock bias values ($> 3 \times 10^3$ m) or where
140 the XYZ σ was over 0.1 m; and then rejecting epochs with residuals to a linear trend larger than three standard deviations per coordinate component. The XYZ timeseries were converted to a local east-north-up coordinate frame, detrended and resampled to 30-min sampling rate via a simple 7-point window average (7 samples \rightarrow 1 sample). 30-min averaging reduces high frequency noise (unrelated to OTL) as well as the computational burden of further harmonic analysis.

Finally, OTL displacements modelled in GipsyX were added back using HARDISP (Petit and Luzum, 2010). HARDISP
145 uses spline interpolation of the tidal admittance of 11 major constituents to infer values of 342 tidal constituents and generate a time series of tidal displacements. This approach almost eliminates the effect of companion constituents (Foreman and Henry, 1989) as they are modelled during the processing stage; small errors in the modelled major OTL constituents will propagate into negligible errors in modelled companion tides. Thus, the analysed harmonic displacement parameters represent true displacement plus an indiscernible companion constituent error that is far below the measurement error. We tested the
150 effect of the ‘remove-restore’ OTL procedure we adopted by solutions without modelling OTL in GipsyX. The resulting differences in M_2 amplitudes were smaller than 0.1 mm, and this was reduced further when coordinate process noise was increased. This confirms that the results are independent of the prior FES2004_GBe OTL values. The findings in our paper are provided in the context of GipsyX software and solutions derived using other software may produce different results especially if the underlying model choices differ.

155 The harmonic analysis of the reconstructed OTL signal was performed using the Eterna software v.3.30 (Wenzel, 1996), resulting in amplitudes and local tidal potential phase lags negative which are suitable for solid Earth tide studies. OTL phase-lag, however, is defined with respect to the Greenwich meridian and phase lags are positive. Transforming to Greenwich-relative lags was done according to Boy et al. (2003) and Bos (2000). We then computed the vector difference between the reconstructed observed OTL and that predicted by the model, following the notation of Yuan et al. (2013):

$$160 \quad Z_{res} = Z_{obs} - Z_{th} \quad (1)$$

In Eq. 1 we assume body tide errors to be negligible, thus Z_{obs} is simply an observed OTL and Z_{th} is a theoretical OTL while Z_{res} , the residual OTL, is their vector difference. Z_{res} presented in this publication is, if not otherwise specified, relative to the theoretical OTL values computed using the FES2014b ocean tide atlas, a successor of FES2012 used in Bos et al. (2015), and a Green’s function based on the STW105 Earth model additionally corrected for dissipation at the M_2 frequency which
165 we call STW105d (referred to as FES2014b_STW105d). We utilize box-and-whisker plots to visualise the distribution of the estimates with the box and whiskers defined as the inter-quartile range (IQR) and an additional $\pm 1.5 \times \text{IQR}$, respectively, with the median as a horizontal line.

4 Process noise optimization

Process noise settings within GipsyX need to be chosen to ensure optimal separation of site displacement, tropospheric zenith delays, noise etc. For example, a tight coordinate process noise value, even the default value of 0.57 mm/sqrt(s), tends to clip OTL amplitudes, especially in coastal sites. Penna et al. (2015) developed a method of tuning process noise values for GPS PPP, which we expanded to accommodate the additional major diurnal/semidiurnal constituents considered here, as well as the use of both GPS and GLONASS data.

To do this, we used the CAMO site, the successor of CAMB used by Penna et al. (2015) and tested a range of coordinate and Zenith Wet Delay (ZWD) process noise settings exactly as described by Penna et al. (2015). We perform separate tests for GPS only, GLONASS only and GPS+GLONASS solutions. These tests focus on a range of metrics, namely the standard deviation of the height time series (shown as “Ht std/3”, as divided by 3), the standard deviation of kinematic ZWD normalized by ZWD values from a static solution (“ZWDstatic”), root mean square of the carrier phase residuals (“RMSres”), M_2 residual OTL magnitude, $\|Z_{res}\|$, and $\|Z_{res}\|$ of a synthetic ~ 13.96 h signal and its controlled, known input (designated “synth err”). We focus on the results without the introduction of this synthetic signal here.

For each of the major constituents, both diurnal and semi-diurnal, and for each of the constellation choices, we found that 3.2 mm/sqrt(s) for coordinate process noise and 0.1 mm/sqrt(s) for tropospheric zenith delay process noise were optimal for our solutions, the same values as identified by Penna et al. (2015) for M_2 using GPS only. Figure 2 shows the results of the tests, with the left panel showing the result of varying coordinate process noise while ZWD process noise was held fixed (0.1 mm/sqrt(s), a default value) and the right panel the result of varying the ZWD process noise with coordinate process noise equal to the optimum value of 3.2 mm/sqrt(s). The finding of identical optimal process noise settings for all constituents and constellations suggests that the different amplitudes and frequencies are less important than the data noise in the semidiurnal and diurnal frequency bands and that the constellation-specific data noise does not substantially vary between constellations.

5 Results and Discussion

Given the known accuracy of the ocean tide models in this region (Penna et al., 2015), and small effects of errors in solid Earth models, our assumption is that as $\|Z_{res}\|$ approaches zero as the estimates increase in accuracy, also shown by Bos et al. (2015). Based on previous studies (e.g., Yuan et al., 2013) we expected $\|Z_{res}\|$ median values (up component) of ~ 2 mm for K_2 and K_1 , ~ 1 mm for M_2 , S_2 , P_1 and ~ 0.5 mm for N_2 , O_1 , Q_1 .

Figure 3 (upper panel) shows GPS, GLONASS and GPS+GLONASS $\|Z_{res}\|$ estimates for each of the east, north and up coordinate components. Over all components, the $\|Z_{res}\|$ are uniformly small for N_2 , O_1 and Q_1 , with median around 0.1 mm. Residuals are slightly higher for M_2 , P_1 and S_2 , median being around 0.5-0.7 mm, and are often noticeably higher for K_1 and K_2 although there is substantial variation by constellation.

The combined GPS+GLONASS solutions perform either at the same level as GPS AR (M_2 , O_1 , Q_1) or better (N_2 , P_1) for the up component. $\|Z_{res}\|$ values are smaller and more consistent for the east (M_2 , N_2 , O_1) and north (M_2 , N_2 , P_1) components respectively. The GPS+GLONASS solution does not have $\|Z_{res}\|$ biases in the east and north components as is

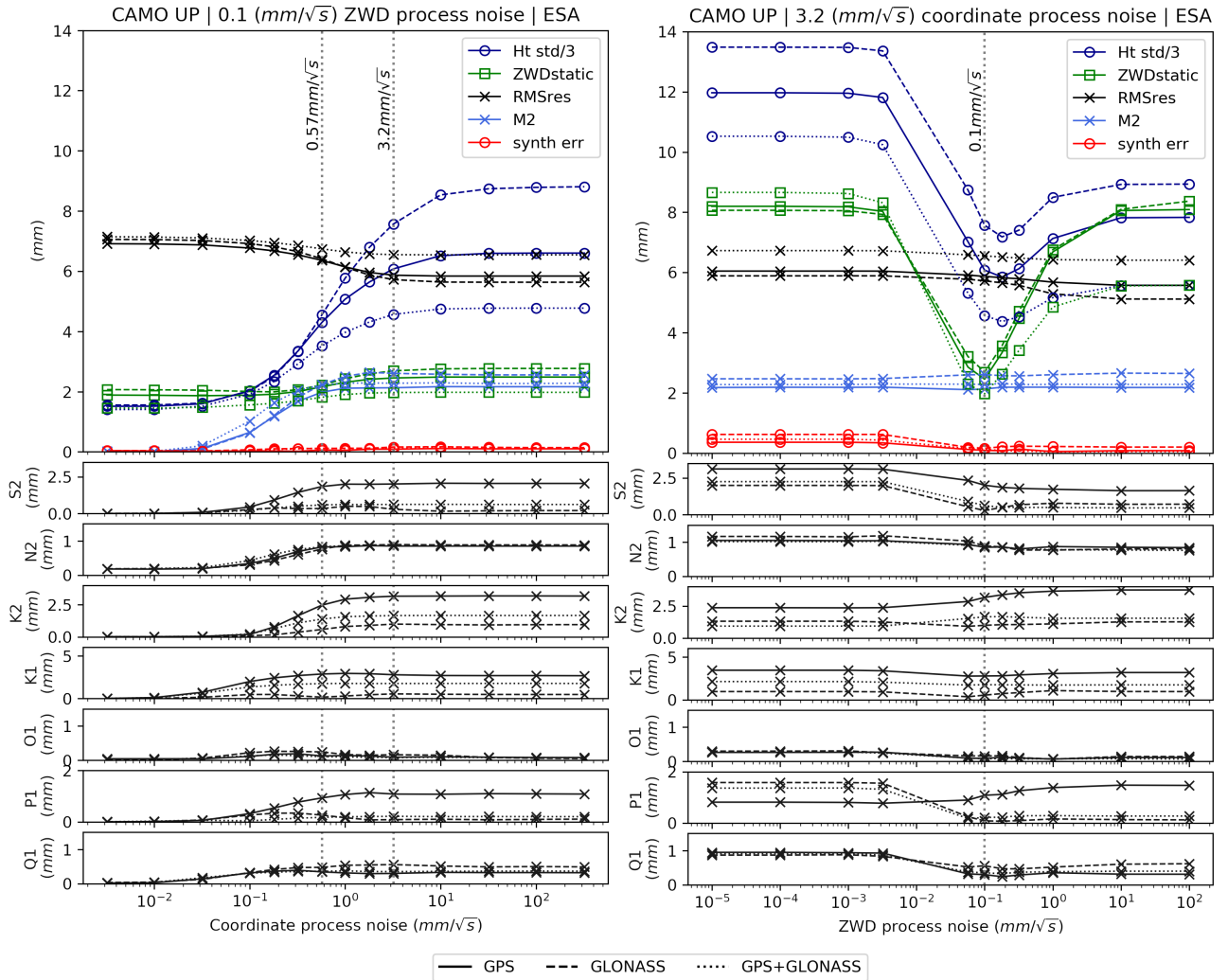


Figure 2. The effect of varying coordinate process noise (left) and ZWD process noise (right) at test site CAMO for the up component (2010.0 – 2014.0), performed with ESA repro2 products. $\|Z_{res}\|$ is relative to FES2004_GBe. The different constellations' configurations: GPS, GLONASS and GPS+GLONASS are presented as solid, dashed and dotted lines respectively. The colours pertain to the different metrics as described in the text and legend (note the same scheme is used as per Penna et al. (2015)).

noticeable for the GPS AR solution (particularly for O_1 in east, and P_1 in north, respectively). By $\|Z_{res}\|$ bias we mean a noticeable gap between zero and the lower whisker.

Considering the problematic GPS K_2 and K_1 constituents, the GPS AR can reasonably reliably, in comparison to other types of solutions, extract $\|Z_{res}\|$ in the east component (Figure 3, lower left panel) which is smaller than that of GLONASS and GPS+GLONASS using ESA or CODE products. However, smallest $\|Z_{res}\|$ in the up and north components is possible

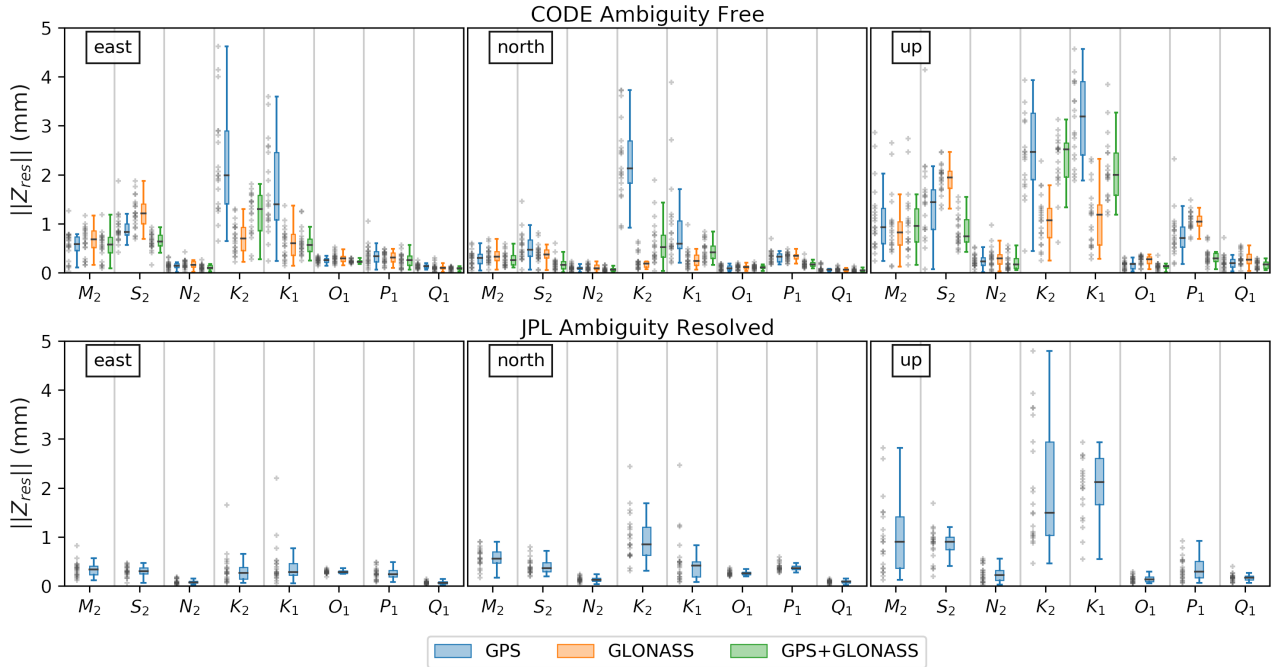


Figure 3. $\|Z_{res}\|$ per tidal constituent for east, north and up components (left, middle and right, respectively) relative to FES2014b_STW105d OTL values with CMC correction for JPL solutions. Grey crosses to the left of each boxplot represent sites' $\|Z_{res}\|$ values and are offset horizontally for clarity while the horizontal line over each boxplot is a median of each constituent's $\|Z_{res}\|$. Top: $\|Z_{res}\|$ for GPS, GLONASS and GPS+GLONASS PPP solutions (blue, orange and green, respectively) computed using CODE products. Bottom : $\|Z_{res}\|$ of the GPS AR solution computed with JPL native products. The boxes show the inter-quartile range and the whiskers mark the limit of an additional $\pm 1.5 \times \text{IQR}$, with median as a horizontal line

only using the GLONASS constellation solely which aligns with the conclusions of Abbaszadeh et al. (2020) who used ESA products and globally distributed GNSS network of sites.

Our results suggest that no single solution provides consistently better constituent estimates across all coordinate components. We suggest that optimum results are obtained using GPS+GLONASS for M_2 , S_2 , N_2 , O_1 , P_1 and Q_1 , and GLONASS for K_2 and K_1 , noting that GPS AR performs better for all constituents in the east component.

We now explore the sensitivity of our solutions to different products and analysis choices starting with elevation cutoff angle sensitivity, which particularly affects the amount of multipath influence on the coordinate time series. We pay particular attention to S_2 , K_2 , P_1 and K_1 given the large systematic errors evident in GPS only solutions. We follow with an inter-comparison of solutions using various products and then assess the impact of integer ambiguity resolution (GPS only). Finally, we test the stability of the constituent estimates to time series length.

5.1 Satellite orbit and clock products sensitivity tests

We assessed whether the solutions were sensitive to changes in satellite-elevation cutoff angle. Three additional cutoff angle scenarios were tested: 10°, 15° and 20° (in addition to the default 7° cutoff angle). Different elevation angle cutoffs will significantly alter the observation geometry as well as modulate the expression of signal multipath into solutions, decreasing the likely influence of multipath with higher cutoff values.

Figure 4 (top) shows the magnitude of vector difference, $\|\Delta Z_{res}\|$, between Z_{res} values estimated from the 7° and 20° solutions and CODE products in both cases (upper subplot). S_2 , K_2 , K_1 and P_1 constituents in the up coordinate component show larger mean magnitudes of vector differences in both GPS (0.56, 2.29, 2.88, 0.54 mm, respectively) and GLONASS (0.82, 0.64, 1.01, 0.58 mm, respectively) with the rest of constituents showing differences of less than 0.5 mm. GPS+GLONASS shows the smallest $\|\Delta Z_{res}\|$ between 7° and 20° cutoff estimates for S_2 and P_1 (0.31, 0.23 mm, respectively) and an additional decrease in $\|\Delta Z_{res}\|$ for M_2 , S_2 , N_2 , O_1 , Q_1 in the up component. The high agreement between OTL values indicates the high stability of GPS+GLONASS estimates with changing cutoff angles.

The same comparison for GPS AR (7° and 20° cutoff, JPL native products) shows largely improved stability in comparison to all GPS only ambiguity free solutions (Figure 4, bottom). However, K_2 up and K_1 up show substantial differences between solutions: K_2 shows as much smaller variance of $\|Z_{res}\|$ distribution in the 20° solution, possibly due to removal of multipath, and K_1 shows an increased variance and median of $\|Z_{res}\|$ at increased cutoff angle.

Following Yuan et al. (2013), we assessed the possible influence of inconsistencies in precomputed orbits/clocks on estimated OTL displacements. This was done by computing $\|\Delta Z_{res}\|$ between pairs of solutions with common constellation configurations: GPS (no AR here) solutions computed using ESA, CODE and JPL products; GLONASS/GPS+GLONASS solutions using ESA and CODE products. Figure 5 (top) shows the distribution of $\|\Delta Z_{res}\|$ between solutions computed with ESA and CODE products for all three constellation modes: GPS, GLONASS and GPS+GLONASS. The main differences are related to the S_2 , K_2 , K_1 and P_1 constituents. The maximum $\|\Delta Z_{res}\|$ between the observed OTL for the rest of the constituents is less than ~ 0.3 mm.

Compared with GPS JPL, both CODE and ESA solutions (Figure 5, middle and bottom, respectively) show $\|\Delta Z_{res}\|$ up to 0.5 mm in the horizontal components with respect to JPL solutions, which is also true for ESA in the up component with exception for K_2 and K_1 . CODE shows similar behaviour to ESA, however, significant divergence from JPL (Figure 5, middle) is also observed for S_2 with even higher $\|\Delta Z_{res}\|$ for K_2 and K_1 in the up and the east.

5.2 S_2 constituent

Focusing on S_2 , the GPS up residual shows ~ 1 mm residual bias between solutions using CODE and ESA products (compare blue records between left and right panels, Figure 6). The GPS $\|Z_{res}\|$ bias remains for solutions with a range of elevation cutoff angles (7°, 10°, 15° and 20°). GLONASS solutions (orange), however, show no $\|Z_{res}\|$ bias for ESA and ~ 1.5 mm bias for CODE, both with 7° elevation angle. GLONASS bias values with both products increase with elevation cutoff angle up to

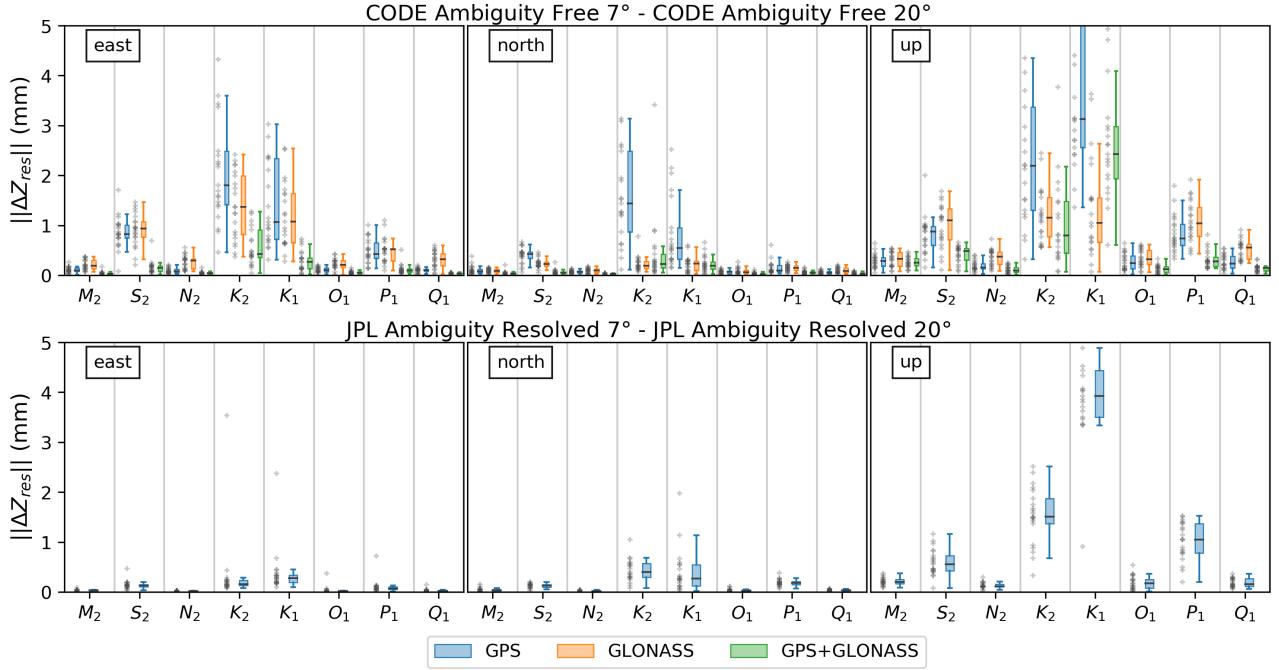


Figure 4. Magnitude of vector difference between estimated Z_{res} values computed with 7° and 20° elevation cutoff angles, $\|\Delta Z_{res}\|$, within the same set of orbits and clocks (top: CODE; bottom: JPL AR) for east, north and up coordinate components (left, middle and right, respectively). Grey crosses are as per figure 3. The smaller residuals using CODE products with GPS+GLONASS (top) is a result of improved OTL stability as a function of cutoff angle using combined constellations (except K_1 up and K_2 up). JPL’s GPS AR also shows great stability with exception of K_2 up and K_1 up. $\|\Delta Z_{res}\|$ for GPS, GLONASS and GPS+GLONASS PPP solutions in blue, orange and green, respectively.

15° . This GLONASS dependency with elevation cutoff is present to a lesser degree in both east and north components and is the same with ESA and CODE products (Fig. S5).

250 GPS $\|Z_{res}\|$ estimates show similar behaviour in terms of $\|Z_{res}\|$ bias between ESA and CODE solutions in the up component (blue, Figure 6) but ESA solutions’ median $\|Z_{res}\|$ values are ~ 1 mm larger for all elevation cutoff angle solutions. Both ESA and CODE GPS+GLONASS S_2 results (green, Figure 6) show a blend of the two patterns observed with GPS and GLONASS solutions. GPS+GLONASS S_2 shows less sensitivity to the cutoff angle change than GLONASS or GPS solutions alone.

255 The substantial difference in S_2 between ESA and CODE (Figure 6) suggests important differences in raw GNSS data analysis approaches within respective Analysis Centres. One relevant difference between products is in treatment of S_1 and S_2 atmospheric tides which were corrected for at the observation level in CODE products but not in ESA. However, the inverse behaviour of GPS and GLONASS between ESA and CODE solutions (orange, Figure 6) cannot be explained with a

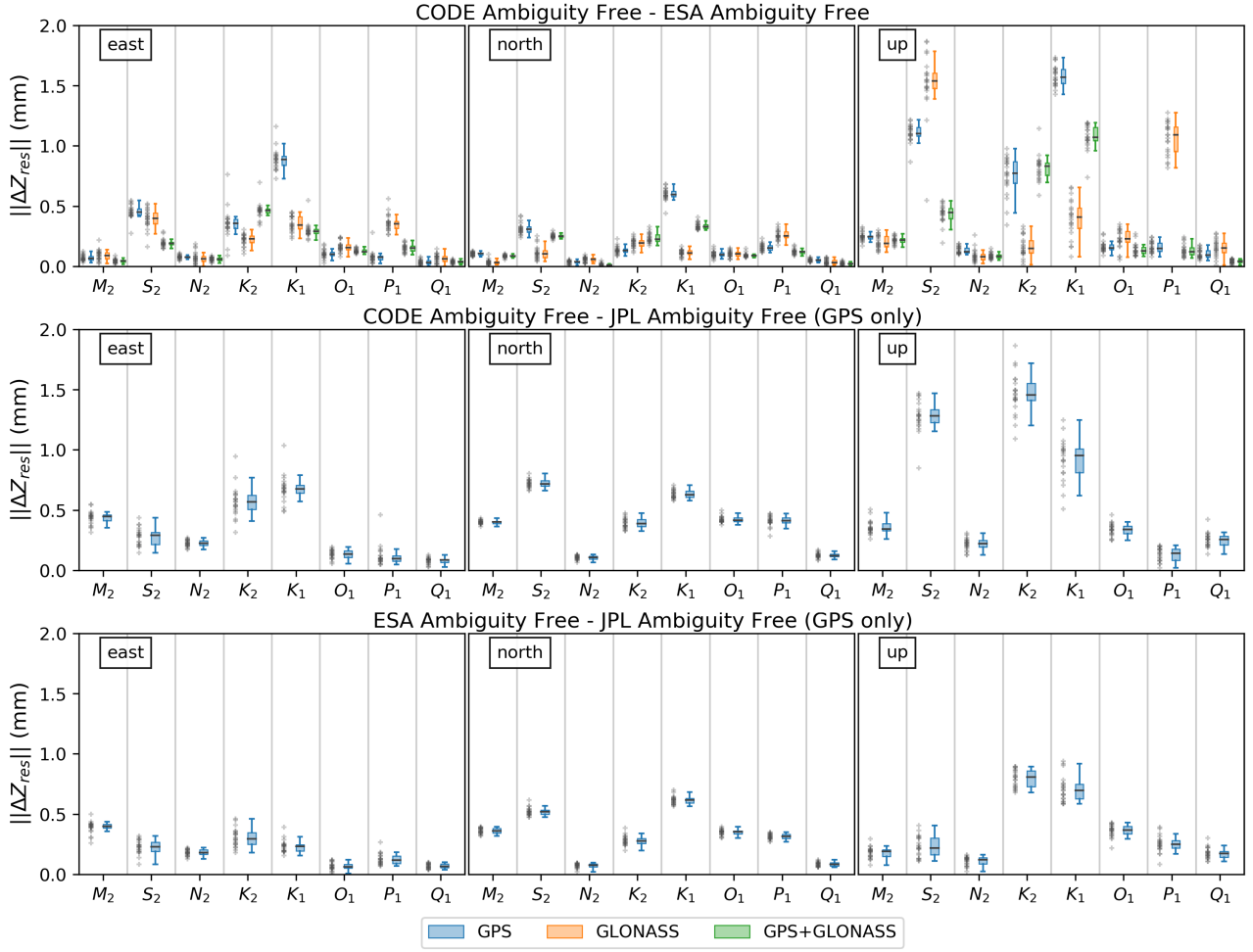


Figure 5. OTL vector differences between CODE, ESA and JPL solutions (ambiguity free). Top: GPS, GLONASS and combined GPS+GLONASS differences between CODE and ESA solutions; Middle: GPS difference between CODE and JPL solutions (ambiguity free); Bottom: GPS difference between ESA and JPL solutions (ambiguity free). Note the vertical scale of 2 mm. Grey crosses are as per Figure 3.

single correction applied to both constellations. We expect that the differences in each solution are a function of satellite orbit
 260 modelling, although the exact origin is not clear and needs further investigation.

5.3 K_2 and K_1 constituents

As seen from Fig. 3, $\|Z_{res}\|$ can be minimized if using GLONASS for the extraction of K_1 and K_2 constituents and GPS+GLONASS for the remainder of the constituents. In this case, $\|Z_{res}\|$ will stay below 0.25 mm for north components and below 0.5 mm for the east and the up components.

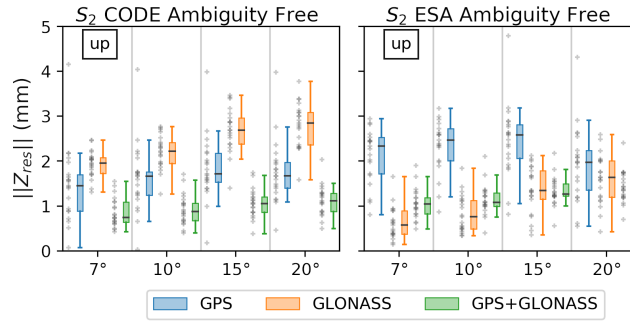


Figure 6. GPS, GLONASS and GPS+GLONASS $\|Z_{res}\|$ for the S_2 constituent in the up component as a function of elevation cutoff angle, computed with ESA (left) and CODE products (right). Note the inverse behaviour of GPS and GLONASS biases and the linear dependence of the GLONASS biases. Grey crosses are as per Fig. 3.

265 GLONASS K_2 and K_1 estimates in the north have the lowest variance in $\|Z_{res}\|$ and are most stable with different elevation cutoff angles and products. For the east component, CODE products with GLONASS have larger $\|Z_{res}\|$ median and scatter than with GPS+GLONASS for K_1 and in terms of elevation cutoff stability (K_2 and K_1). Solutions using the ESA GLONASS products, however, perform better for K_1 east than the respective GPS+GLONASS in terms of $\|Z_{res}\|$ distribution consistency and median (Fig. S2). Elevation cutoff stability of ESA K_2 and K_1 in the east component is best with GPS+GLONASS as also
270 found when using CODE products.

The up component of K_2 and K_1 is the most problematic, showing high $\|Z_{res}\|$ values with all constellation modes. GLONASS OTL values using either both ESA or CODE products have the smallest medians and variances of $\|Z_{res}\|$, outperforming JPL GPS AR. Note that GPS+GLONASS K_2 up has a marginally smaller median $\|\Delta Z_{res}\|$ in the elevation cutoff test than that of GLONASS only, possibly due to the larger number of total satellites, however, both K_2 and K_1 $\|Z_{res}\|$ suggest a
275 ~ 1.5 mm bias.

While we cannot definitively select a single constellation configuration optimal for all components of K_2 and K_1 , we can conclude that based on our analysis, GLONASS solutions have smaller $\|Z_{res}\|$ in the K_2 and K_1 north and up components while the east component shows better results with GPS+GLONASS (K_1 , CODE). However, we recommend GLONASS-only solutions due to the higher level of agreement between solutions using ESA and CODE products. The only exception is the
280 east component where the preference is for JPL GPS AR (see Sect. 5.7).

5.4 P_1 constituent

GLONASS P_1 constituents show high $\|\Delta Z_{res}\|$ between CODE and ESA solutions over all coordinate components (orange, Figure 5 top). This was unexpected as ESA and CODE $\|Z_{res}\|$ boxplots show similar distributions of values (see Figure S2 in the supplementary material for the equivalent ESA boxplots). This suggests a symmetrical deviation from the modelled values
285 that produces a high $\|\Delta Z_{res}\|$. In all cases, however, GPS+GLONASS is preferred for P_1 estimation.

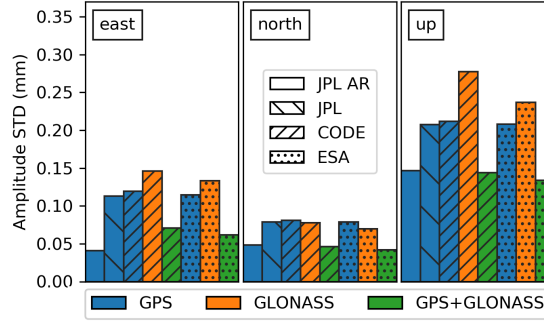


Figure 7. Average uncertainties (1-sigma) for OTL amplitudes computed across eight OTL constituents per products (stipple) and processing modes/constellation (colour): GLONASS (orange) and GPS (blue) modes show higher 1-sigma uncertainties, while GPS-only AR and combined GPS+GLONASS (green) show minimum 1-sigma uncertainties with exception for east.

5.5 Effect of different orbit and clock products on noise and uncertainty

Changing orbit and clock products also changes the time series noise characteristics and hence influences the uncertainties of the estimated constituents (estimated separately by Eterna for amplitude, Figure 7 and phase, Figure 8). Amplitude uncertainties are expressed here as an average across all constituents as they do not differ much between analysed constituents. ETERNA
 290 assumes a white noise model in its analysis. We conclude that GLONASS solutions produce the highest amplitude uncertainties for east (0.15 mm CODE, 0.14 mm ESA) and up components (0.22 mm CODE, 0.27mm ESA) while showing the same uncertainty as GPS for the north (0.07 mm, both CODE and ESA). GLONASS solutions using CODE products tend to have amplitude uncertainties that are marginally higher than those of ESA products. The amplitude uncertainties for combined GPS+GLONASS solutions are equal to those of JPL with ambiguities fixed (GPS AR), although the JPL GPS AR solution has
 295 slightly smaller uncertainty in the east component (smaller by ~ 0.02 mm).

Considering the uncertainties of phase values, these are unsurprisingly dependent on the constituent's amplitude. Because JPL native products are in a CM frame, the constituent amplitudes are larger at the time of ETERNA analysis than those using ESA and CODE products which are both provided in a CE frame. For the ESA and CODE solution, this results in up to an order of magnitude increase in phase uncertainties for “weaker” diurnal constituents in the region: N_2 , O_1 , P_1 , Q_1 (Figure 8).
 300 In general, this frame effect is directly related to centre of mass correction (CMC) specific to the constituent's CMC vector in comparison to the total theoretical OTL vector. If applying a CMC correction to the constituent increases its amplitude, phase STD values will decrease in a CM frame solution. This is critically important for the constituents with amplitudes below 0.5 mm, as phase uncertainty increases significantly below this threshold. The most significant exception in our dataset is P_1 in the up component which has a much larger amplitude in CE frame (Figure 8, right in top and bottom).

305 Converting CE products to CM (Figure 8, bottom) was done to demonstrate that the changes in phase uncertainty are indeed introduced by the smaller amplitudes in the CE frame. While this holds true, it is obvious that the P_1 up phase uncertainty increases, as was expected based on comparison with the JPL solutions. GLONASS K_1 up phase uncertainties show almost

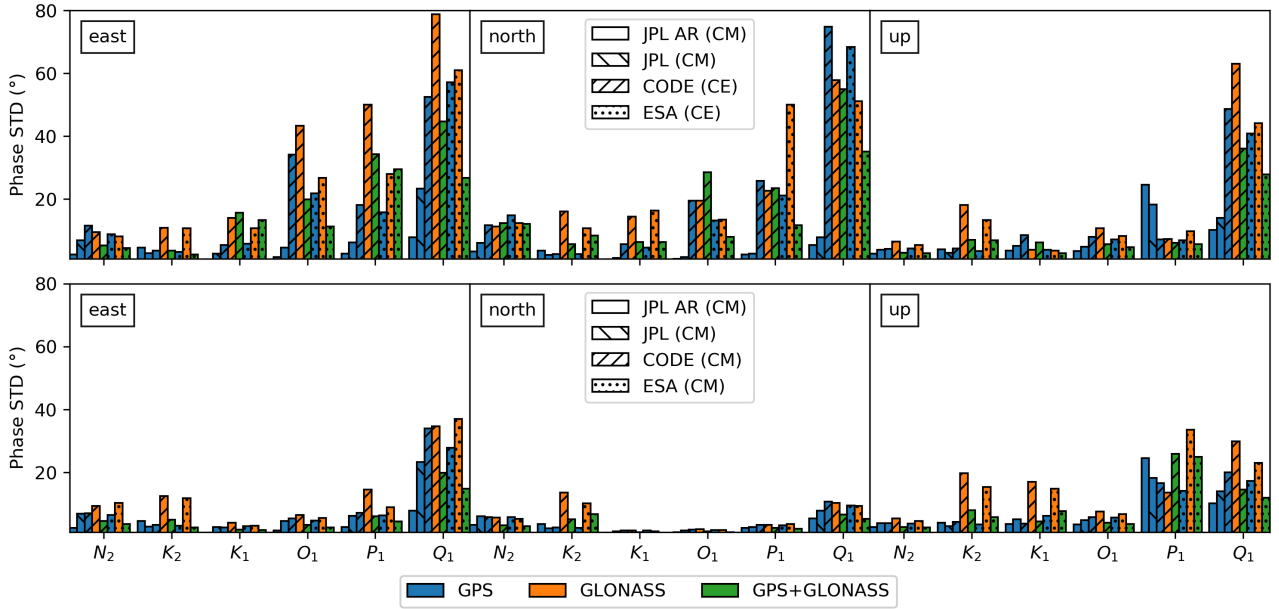


Figure 8. Average phase uncertainty per constituent for different products as returned by Eterna. ESA and CODE products were in CE frame by default (top) and converted to CM (bottom) while JPL are in CM in both. M_2 and S_2 phase 1-sigma uncertainties are not shown here as values are too small to be seen with the scale specified.

an order of magnitude increase in the CM frame while having unexpectedly small values in CE. This is a direct cause of GLONASS solution having larger K_1 up amplitudes in CE and smaller in CM with both CODE and ESA.

310 5.6 Impact of Ambiguity Resolution on GPS

The multi-GNSS products used here do not allow integer AR with PPP and this is an active area of research and development within the IGS. However, assessing the impact of AR on GPS-only solutions provides some insight towards the future benefit of AR on GLONASS and GPS+GLONASS solutions once such products become available. We compared OTL residuals from GPS and GPS AR using JPL native products that contain wide lane and phase bias tables (WLPB files) required for integer AR with PPP.

Figure 9 shows the effect on estimated constituents from enabling AR in a standard solution with 7° cutoff. Here we observe decreased $\|Z_{res}\|$ over all coordinate components compared with the estimates from a non-AR solution. This is most visible in the K_2 and K_1 constituents and in the elimination of the S_2 $\|Z_{res}\|$ bias and with smaller improvements in M_2 and P_1 .

Importantly, Figure 9 shows that enabling AR eliminates $\|Z_{res}\|$ bias in GPS and aligns the residual vectors with ESA/CODE GPS+GLONASS (Figure 3). This is a clearer improvement than reported by Thomas et al. (2006).

Given this effect, the S_2 $\|Z_{res}\|$ bias was once again assessed with various elevation cutoff angles solutions. JPL GPS solutions (floating AR), in the up component (Figure 10, left), show the S_2 $\|Z_{res}\|$ bias to be constant with cutoff angle, being

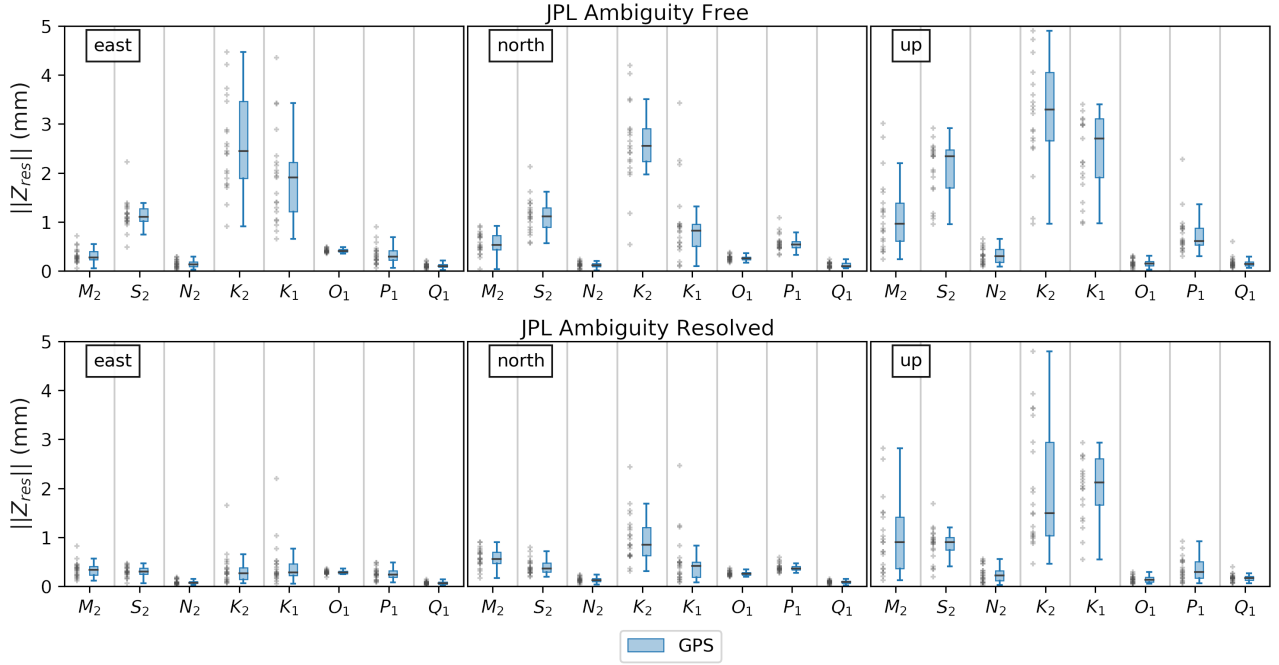


Figure 9. Comparison of residual constituents' estimates from GPS (top) and GPS AR (bottom) JPL native solutions. Grey crosses are as per Figure 3. As seen, most of constituents' $\|Z_{res}\|$ distribution variances and medians are smaller while S_2 $\|Z_{res}\|$ bias is removed with AR solutions.

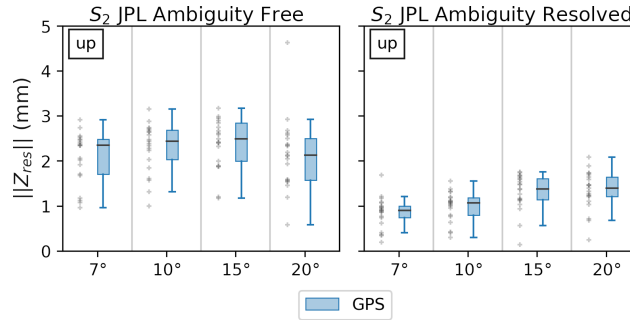


Figure 10. GPS S_2 up constituent's $\|Z_{res}\|$ change with elevation cutoff angle computed with JPL products floating AR (left) and integer AR (right). Grey crosses are as per Figure 3. As seen, AR helps in removing the bias and decreases the $\|Z_{res}\|$ distribution variance.

about 1 mm, and with the $\|Z_{res}\|$ variance of around 3 mm. Similar behaviour was previously observed with solutions using ESA products (Fig.6).

325 Enabling integer ambiguity resolution (GPS AR) removes the ~ 1 mm S_2 $\|Z_{res}\|$ bias completely at 7° and 10° elevation cutoff angles while leaving ~ 0.4 mm bias at 15° and 20° in the up component. Consequently, up $\|Z_{res}\|$ medians change by 1-2 mm depending on elevation cutoff angle. Based on this observation, we expect that resolving ambiguities within PPP

might help in solving, or at least minimising, the $S_2 \|Z_{res}\|$ present in ESA GPS and CODE GLONASS solutions. Eliminating biases in GPS and GLONASS separately should increase the stability and consistency of GPS+GLONASS $S_2 \|Z_{res}\|$.

330 5.7 Impact of timeseries length

Yuan et al. (2013) used a filter based harmonic parameter estimation approach and examined the dependence of Kalman filter convergence on timeseries length for each of the eight major constituents. Yuan et al. (2013) concluded that, after 1000 daily solutions, convergence (minimized $\|Z_{res}\|$) was reached for lunar-only constituents (M_2 , N_2 , O_1 , Q_1) while reporting solar-related constituents (S_2 , K_2 , K_1 , P_1) were not fully converged even after 3000 daily solutions.

335 We assessed how $\|Z_{res}\|$ of each of 8 major constituents vary as a function of the time series length with kinematic estimation approach. The duration of the series varied by integer years and, to enable a complete analysis, we expanded the candidate solutions to 2019.0 and processed additional data with operational products: JPL repro3.0, ESA operational, CODE MGEX (CODE operational lack GLONASS clock corrections). While the goal of a reprocessing campaign is to preserve consistency with operational products (Griffiths, 2019), based on previous results, we assumed that changing satellite orbit and
340 clock products may produce substantial differences in problematic solar-related constituents (S_2 , K_2 , K_1 , P_1). Thus, we first performed a comparison of ESA repro2 solutions (2010.0-2014.0) with the ESA operational product (2014.0-2019.0) which confirmed the hypothesis (Figure 11). GLONASS $\|\Delta Z_{res}\|$ show the smallest variance for K_1 and K_2 compared with GPS and GPS+GLONASS but are significant, up particularly, which might be related to the changes in the analysis used to produce GLONASS orbits and clocks. Considering S_2 , the very same form of bias remains as previously seen in the 2010.0-2014.0
345 dataset. This suggests a symmetric deviation of repro2 and operational products solutions from the modelled value. The same explanation can be applied to the GPS-only $P_1 \|\Delta Z_{res}\|$ bias in the up component of 0.5 mm.

The results shown in Figure 12 are produced from a composition of reprocessed products and operational products (years 5 to 9). We focus on S_2 up and K_1 up, as the most problematic diurnal constituents. The results align with general conclusions of Yuan et al. (2013) suggesting a weak relationship between timeseries length and $\|Z_{res}\|$ for solar-related constituents.
350 However, if constituents are examined according to our recommended optimum constellation strategy, $\|Z_{res}\|$ appears (see Fig. S4) stable over time, which suggests that even if there are changes in the products, they are not having an impact with this methodology.

6 Conclusions

We expand the GPS-only methodology of ocean tide loading displacement estimation described in Penna et al. (2015) with data
355 from the GLONASS constellation. We assess the performance of GPS and GLONASS for the estimation of eight major ocean tide loading constituents in stand-alone modes and in a combined GPS+GLONASS mode. We examine data from 21 sites from the UK and western Europe over a period of 2010.0-2014.0 through processing data in kinematic PPP using products from three different analysis centres: CODE, ESA and JPL. The latter was also used to assess the effect of GPS ambiguity fixing on estimated ocean tide loading displacements. All solutions were inter-compared to gain an insight into the sensitivities of

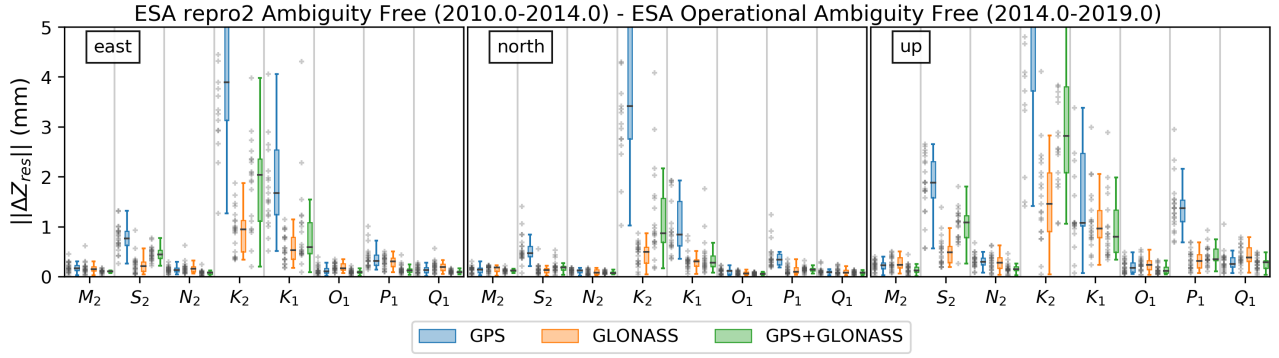


Figure 11. OTL vector differences between ESA repro2 (2010.0-2014.0) and ESA operational (2014.0-2019.0) OTL estimates: GPS (blue), GLONASS (orange), GPS+GLONASS (green) constellation modes present. Grey crosses are as per Figure 3.

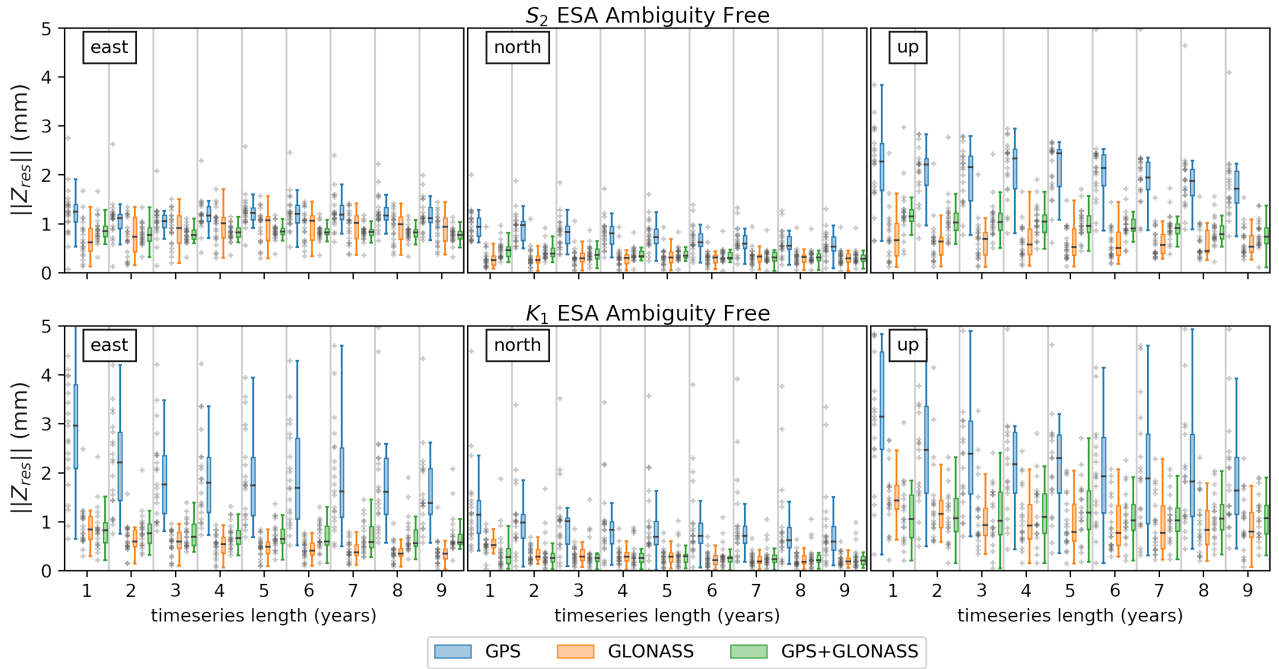


Figure 12. Dependency of estimated $\|Z_{res}\|$ and timeseries' length in years for two solar related constituents: S_2 (top), K_1 (bottom). GPS, GLONASS and GPS+GLONASS PPP solutions in blue, orange and green, respectively using ESA products. Grey crosses are as per Figure 3. Note that 1 to 4 years of timeseries length use ESA repro2 while the rest uses a combination of ESA repro2 and ESA operational products.

360 the constituent estimates to different choices of satellite orbit and clock products, satellite elevation cutoff, and constellation configurations.

We find that the optimal constellation mode varies across all eight major tidal constituents and components. We show that ambiguity-free GPS+GLONASS solutions show a similar level of precision as GPS with ambiguities resolved (GPS AR), with P_1 estimates using GPS+GLONASS showing improved precision and stability. The K_2 and K_1 constituents, which are known to be problematic in GPS solutions, are still unusable in GPS+GLONASS solutions, presumably due to the propagation of GPS related errors. The S_2 constituent also cannot be reliably recovered with GPS+GLONASS as GLONASS shows dependency between the estimates and the chosen elevation cutoff angle. GPS-based estimates of S_2 show a constant bias in absolute residuals when ambiguity resolution is not implemented, but this is substantially reduced by resolving the ambiguities to integers. GLONASS-based estimates show a comparable level of performance to ambiguity-free GPS for M_2 , N_2 , O_1 , P_1 and Q_1 while showing improved results for K_2 and K_1 .

Additional comparison of OTL estimates from reprocessed and operational products shows that GLONASS estimates of K_2 and K_1 show differences in the up and, to the lesser extent in the east, components when using different products.

Considering the above, we suggest that estimation of K_1 and K_2 constituents is best undertaken using GLONASS only solutions with an emphasis towards the north component where it is most stable. M_2 , S_2 , N_2 , O_1 and Q_1 can be reliably estimated from combined GPS+GLONASS or GPS AR solutions while P_1 is best with GPS+GLONASS.

Integer ambiguity resolution was not possible in the GLONASS or GPS+GLONASS solutions tested here due to limitations in the products available. However, evidence from our GPS AR testing suggests that further increases in precision and stability will be seen when AR fixing can be performed using GLONASS, and this should have a positive impact on estimates of solar-related constituents.

Code and data availability. GNSS data were obtained from the Natural Environment Research Council (NERC) British Isles continuous GNSS Facility (BIGF), www.bigf.ac.uk and the International GNSS Service (IGS), www.igs.org. OTL values and TPXO7.2 OTL grid were obtained from free ocean tide loading provider, holt.oso.chalmers.se/loading/. CODE REPRO_2015 and CODE MGEX orbit and clock products were obtained from the University of Bern, ftp.aiub.unibe.ch/REPRO_2015/ and ftp.aiub.unibe.ch/CODE_MGEX/ respectively, ESA repro2 and operational from the Crustal Dynamics Data Information System (CDDIS), JPL repro 2.1 and repro 3.0 from NASA Jet Propulsion Laboratory, sideshow.jpl.nasa.gov/pub/.

GipsyX binaries were provided under license from JPL. Eterna tidal analysis and prediction software with source code was acquired from International Geodynamics and Earth Tide Service (IGETS), igets.u-strasbg.fr/soft_and_tool.php. The source code of GipsyX wrapper developed to facilitate the processing, analyse output and undertake plotting can be found at: github.com/bmatv/GipsyX_Wrapper.

Author contributions. BM facilitated processing of the GNSS data with GipsyX and analysis of the resulting timeseries under the supervision of MK and CW. All authors contributed to the discussion of the results and writing of the manuscript.

Competing interests. The authors declare that they have no conflicts of interest.

Acknowledgements. The services of the Natural Environment Research Council (NERC) British Isles continuous GNSS Facility (BIGF), www.bigf.ac.uk, in providing archived GNSS data to this study, are gratefully acknowledged. We are grateful to NASA Jet Propulsion Laboratory for the GipsyX software, products and support. We thank IGS, www.igs.org, for providing GNSS data and ESA reprocessed products; CODE, www.aiub.unibe.ch, for providing reprocessed products. We thank Klaus Schueller for advice and discussion on Eterna software. The services of TPAC High Performance Computing Facility are acknowledged gratefully. We gratefully acknowledge Machiel Bos whose support and discussion were vital for the project. We thank the Free Ocean Loading Provider for the OTL computation services and for providing the OTL grid that was used in Figure 1.

References

- 400 Abbaszadeh, M., Clarke, P. J., and Penna, N. T.: Benefits of combining GPS and GLONASS for measuring ocean tide loading displacement, *Journal of Geodesy*, 94, 63, <https://doi.org/10.1007/s00190-020-01393-5>, 2020.
- Agnew, D. C.: *Earth Tides*, pp. 151–178, <https://doi.org/10.1016/b978-0-444-53802-4.00058-0>, 2015.
- Allinson, C. R.: Stability of direct GPS estimates of ocean tide loading, *Geophysical Research Letters*, 31, <https://doi.org/10.1029/2004gl020588>, 2004.
- 405 Baker, T. F.: Tidal Deformations of the Earth, *Science Progress*, 69, 197–233, 1984.
- Bar-Sever, Y. E., Kroger, P. M., and Borjesson, J. A.: Estimating horizontal gradients of tropospheric path delay with a single GPS receiver, *Journal of Geophysical Research: Solid Earth*, 103, 5019–5035, <https://doi.org/10.1029/97jb03534>, 1998.
- Bertiger, W., Desai, S. D., Haines, B., Harvey, N., Moore, A. W., Owen, S., and Weiss, J. P.: Single receiver phase ambiguity resolution with GPS data, *Journal of Geodesy*, 84, 327–337, <https://doi.org/10.1007/s00190-010-0371-9>, 2010.
- 410 Boehm, J., Werl, B., and Schuh, H.: Troposphere mapping functions for GPS and very long baseline interferometry from European Centre for Medium-Range Weather Forecasts operational analysis data, *Journal of Geophysical Research: Solid Earth*, 111, <https://doi.org/10.1029/2005jb003629>, 2006.
- Bos, M. S.: *Ocean Tide Loading Using Improved Ocean Tide Models*, Thesis, University of Liverpool, 2000.
- Bos, M. S. and Baker, T. F.: An estimate of the errors in gravity ocean tide loading computations, *Journal of Geodesy*, 79, 50–63, <https://doi.org/10.1007/s00190-005-0442-5>, 2005.
- 415 Bos, M. S., Penna, N. T., Baker, T. F., and Clarke, P. J.: Ocean tide loading displacements in western Europe: 2. GPS-observed anelastic dispersion in the asthenosphere, *Journal of Geophysical Research-Solid Earth*, 120, 6540–6557, <https://doi.org/10.1002/2015jb011884>, 2015.
- Boy, J. P., Llubes, M., Hinderer, J., and Florsch, N.: A comparison of tidal ocean loading models using superconducting gravimeter data, *Journal of Geophysical Research: Solid Earth*, 108, <https://doi.org/10.1029/2002jb002050>, 2003.
- 420 Dziewonski, A. M. and Anderson, D. L.: Preliminary reference Earth model, *Physics of the Earth and Planetary Interiors*, 25, 297–356, [https://doi.org/10.1016/0031-9201\(81\)90046-7](https://doi.org/10.1016/0031-9201(81)90046-7), 1981.
- Farrell, W. E.: Deformation of the Earth by surface loads, *Reviews of Geophysics*, 10, <https://doi.org/10.1029/RG010i003p00761>, 1972.
- Foreman, M. G. G. and Henry, R. F.: The harmonic analysis of tidal model time series, *Advances in Water Resources*, 12, 109–120, [https://doi.org/10.1016/0309-1708\(89\)90017-1](https://doi.org/10.1016/0309-1708(89)90017-1), 1989.
- 425 Fu, Y., Freymueller, J. T., and van Dam, T.: The effect of using inconsistent ocean tidal loading models on GPS coordinate solutions, *Journal of Geodesy*, 86, 409–421, <https://doi.org/10.1007/s00190-011-0528-1>, 2012.
- Griffiths, J.: Combined orbits and clocks from IGS second reprocessing, *J Geod*, 93, 177–195, <https://doi.org/10.1007/s00190-018-1149-8>, 2019.
- 430 Griffiths, J. and Ray, J. R.: On the precision and accuracy of IGS orbits, *Journal of Geodesy*, 83, 277–287, <https://doi.org/10.1007/s00190-008-0237-6>, 2009.
- Ito, T. and Simons, M.: Probing asthenospheric density, temperature, and elastic moduli below the western United States, *Science*, 332, 947–51, <https://doi.org/10.1126/science.1202584>, 2011.
- Jentzsch, G.: *Earth tides and ocean tidal loading*, pp. 145–171, Springer-Verlag, <https://doi.org/10.1007/bfb0011461>, 1997.

- 435 Johnston, G., Riddell, A., and Hausler, G.: The International GNSS Service, book section Chapter 33, pp. 967–982, https://doi.org/10.1007/978-3-319-42928-1_33, 2017.
- Khan, S. A. and Tscherning, C. C.: Determination of semi-diurnal ocean tide loading constituents using GPS in Alaska, *Geophysical Research Letters*, 28, 2249–2252, <https://doi.org/10.1029/2000gl011890>, 2001.
- King, M. A.: Kinematic and static GPS techniques for estimating tidal displacements with application to Antarctica, *Journal of Geodynamics*,
440 41, 77–86, <https://doi.org/10.1016/j.jog.2005.08.019>, 2006.
- King, M. A., Penna, N. T., Clarke, P. J., and King, E. C.: Validation of ocean tide models around Antarctica using onshore GPS and gravity data, *Journal of Geophysical Research-Solid Earth*, 110, <https://doi.org/Artn B08401> 10.1029/2004jb003390, 2005.
- Kouba, J.: A guide to using International GNSS Service (IGS) Products, Report, Geodetic Survey Division, Natural Resources Canada, 2009.
- Lau, H. C. P., Mitrovica, J. X., Davis, J. L., Tromp, J., Yang, H. Y., and Al-Attar, D.: Tidal tomography constrains Earth’s deep-mantle
445 buoyancy, *Nature*, 551, 321–326, <https://doi.org/10.1038/nature24452>, 2017.
- Lyard, F., Lefevre, F., Letellier, T., and Francis, O.: Modelling the global ocean tides: modern insights from FES2004, *Ocean Dynamics*, 56, 394–415, <https://doi.org/10.1007/s10236-006-0086-x>, 2006.
- Martens, H. R., Simons, M., Owen, S., and Rivera, L.: Observations of ocean tidal load response in South America from subdaily GPS positions, *Geophysical Journal International*, 205, 1637–1664, <https://doi.org/10.1093/gji/ggw087>, 2016.
- 450 Penna, N. T., Clarke, P. J., Bos, M. S., and Baker, T. F.: Ocean tide loading displacements in western Europe: 1. Validation of kinematic GPS estimates, *Journal of Geophysical Research-Solid Earth*, 120, 6523–6539, <https://doi.org/10.1002/2015jb011882>, 2015.
- Petit, G. and Luzum, B., eds.: IERS Conventions, Verlag des Bundesamts für Kartographie und Geodäsie, Frankfurt am Main, 2010.
- Schenewerk, M. S., Marshall, J., and Dillinger, W.: Vertical Ocean-loading Deformations Derived from a Global GPS Network, *Journal of the Geodetic Society of Japan*, 47, 237–242, <https://doi.org/10.11366/sokuchi1954.47.237>, 2001.
- 455 Stammer, D., Ray, R. D., Andersen, O. B., Arbic, B. K., Bosch, W., Carrère, L., Cheng, Y., Chinn, D. S., Dushaw, B. D., Egbert, G. D., Erofeeva, S. Y., Fok, H. S., Green, J. A. M., Griffiths, S., King, M. A., Lapin, V., Lemoine, F. G., Luthcke, S. B., Lyard, F., Morison, J., Müller, M., Padman, L., Richman, J. G., Shriver, J. F., Shum, C. K., Taguchi, E., and Yi, Y.: Accuracy assessment of global barotropic ocean tide models, *Reviews of Geophysics*, 52, 243–282, <https://doi.org/10.1002/2014rg000450>, 2014.
- Susnik, A., Dach, R., Villiger, A., Maier, A., Arnold, D., Schaer, S., and Jäggi, A.: CODE reprocessing product series, CODE_REPRO_2015,
460 <https://doi.org/10.7892/boris.80011>, http://ftp.aiub.unibe.ch/REPRO_2015/, 2016.
- Thomas, I. D., King, M. A., and Clarke, P. J.: A comparison of GPS, VLBI and model estimates of ocean tide loading displacements, *Journal of Geodesy*, 81, 359–368, <https://doi.org/10.1007/s00190-006-0118-9>, 2006.
- Urschl, C., Dach, R., Hugentobler, U., Schaer, S., and Beutler, G.: Validating ocean tide loading models using GPS, *Journal of Geodesy*, 78, 616–625, <https://doi.org/10.1007/s00190-004-0427-9>, 2005.
- 465 Wang, J., Penna, N. T., Clarke, P. J., and Bos, M. S.: Asthenospheric anelasticity effects on ocean tide loading around the East China Sea observed with GPS, *Solid Earth*, 11, 185–197, <https://doi.org/10.5194/se-11-185-2020>, 2020.
- Wenzel, H.-G.: The nanogal software : Earth tide data processing package ETERNA 3.30, *Bull. Inf. Marées Terrestres*, 124, 9425–9439, 1996.
- Yuan, L. G. and Chao, B. F.: Analysis of tidal signals in surface displacement measured by a dense continuous GPS array, *Earth and Planetary
470 Science Letters*, 355-356, 255–261, <https://doi.org/10.1016/j.epsl.2012.08.035>, 2012.
- Yuan, L. G., Chao, B. F., Ding, X., and Zhong, P.: The tidal displacement field at Earth’s surface determined using global GPS observations, *Journal of Geophysical Research: Solid Earth*, 118, 2618–2632, <https://doi.org/10.1002/jgrb.50159>, 2013.

Zumberge, J. F., Heflin, M. B., Jefferson, D. C., Watkins, M. M., and Webb, F. H.: Precise point positioning for the efficient and robust analysis of GPS data from large networks, *Journal of Geophysical Research: Solid Earth*, 102, 5005–5017, <https://doi.org/10.1029/96jb03860>, 475 1997.